International Journal of Membrane Science and Technology, 2023, Vol. 10, No. 2, pp 3665-3681

Microsturctural Characteristics and Mechanical Properties of Ti 6Al 4V Alloy in Additive Manufacturing

Dhiaa H.Hilfi [1], Suminov Igor [2]

[1] *Department of Mechanical, College of Engineering, University of Misan, Amarah, Iraq. Department of High-Efficiency Processing Technologies, Institute of Production Technologies and Engineering, Moscow state University of Technology "STANKIN", Moscow, Russia.* *diaa.hameed@uomisan.edu.iq*

[2] *Department of High-Efficiency Processing Technologies, Institute of Production Technologies and Engineering, Moscow state University of Technology "STANKIN", Moscow, Russia.* *ist3@mail.ru*

Abstract: Additive manufacturing (AM) is a technique used to create sophisticated tools. This research employs selective laser melting to produce Ti-6Al-4V alloy, followed by after-production heating processes to minimize thermal stress and enhance its mechanical characteristics and microstructure. The study investigates the microstructure, mechanical characterization methodologies, SSRT and SCC advancements, titanium alloy corrosion characteristics, and additive manufacturing of Ti-6Al-4V alloy. This study investigates the mechanical and physical characteristics of additively manufactured Ti-6Al-4V alloy samples, which include tensile strength, elongation, relative density, microhardness, and Young's modulus. This specimen's stress corrosion cracking (SCC) has been assessed using a gradual strain rate test in air and aqueous sodium chloride solutions. The study also examined the effect of thermal processing on the corrosion rates of the Ti-6Al-4V alloy sample produced by the powder bed technique. In phosphate buffer electrolytes and NaCl, corrosion tests were carried out, and the results were compared.

Keywords: Additive manufacturing, microstructural properties, mechanical properties, laser powder bed fusion.

1. INTRODUCTION

1.1 Additive Manufacturing (AM)

The development of new tools and techniques has helped propel additive manufacturing (AM) forward. Powder bed fusion, powder feed processes, and wire feed processes are the three main types of AM metal manufacturing methods (Frazier, 2014). Powder bed fusion, as stated by Leary (2017a), has surface, mechanical, and microstructure qualities that are on par with wrought specimens. Selective laser melting, direct metal laser sintering, electron beam additive manufacturing, and direct metal deposition are among other methods that may be used in this setting (Frazier, 2014).When it comes to producing high-quality components, SLM and DMLS are generally regarded as the most accurate and thoroughly proven methods. There are many different kinds of lasers that may be used for various purposes (Lee et al., 2017); some examples are Nd:YAG lasers, CO2 lasers, excimer lasers, and Yb-fiber lasers. Fast scanning of geometries during SLM and DMLS procedures has been reported using Laser Galvanometer technology, as detailed by Luo et al. (2017). Thin layers of the solid geometry are treated using a laser exposure system that is calibrated to precisely align with the geometric structure being processed. Manufacturing processes using laser sintering fuse metal powder particles at temperatures above their melting point, allowing for the production of solid components through repeated heating and cooling cycles. Additive manufacturing's ability to produce high-quality parts from a variety of materials has led to its rapid adoption in the fields of industrial development and scientific study. Although there are still certain roadblocks to achieving desirable microstructural and mechanical qualities, the technology is making steady progress. Production efficiency should be at the forefront of the suggested industrial solution, with an emphasis on the importance of high levels of accuracy and reproducibility. However, there are still issues that need to be worked out before components can be mass-produced utilising additive manufacturing in terms of form accuracy, consistency, production speed, and load bearing capacity.

1.2 Titanium alloy

The Kroll process is used to create ultra-pure titanium by first purifying the mineral, rutile (TiO2). Once the refined titanium has been prepared, it is put into a fluidized-bed reactor with chlorine gas and carbon to create the final product. Titanium tetrachloride, the byproduct of this procedure, is tainted with contaminants and carbon monoxide. Titanium tetrachloride is purified by heating it in vertical distillation tanks before utilising fractional distillation or precipitation to remove impurities. Argon is supplied into the reactor vessel, where the purified liquid titanium tetrachloride is utilised as a catalyst. Liquid magnesium chloride is produced when magnesium reacts with chlorine after being isolated from solid titanium. Alpha (), Beta (), and alpha-beta (+) alloys are the three types of titanium alloys that are distinguished by the kind of alloying element they include.α *Titanium alloy:* α-titanium alloys excel in welding but cannot be heat treated, making their use in aerospace industry to be limited. They exhibit low to medium strength, moderate notch toughness, and good ductility under cryogenic temperatures.

- $\beta\ Titanium\ alloy:$ Vanadium, tungsten, molybdenum, silicon, and tantalum are used as phase stabilizers in these alloys to increase their resistance and fabricability deformation. These stabilizing substances also improve the ability for heat treatment, enabling significant strengthening. These alloys are easier to make because they have a higher density than pure titanium and a higher strength to modulus of elasticity ratio.
- $(\alpha + \beta) Titanium\ alloy:$ The most commonly used titanium alloy is Ti-6Al-4V, which contains 6% and 4% of aluminum and vanadium, respectively. Vanadium hardens and strengthens the phases, stabilizing the ductile state for extremely high-temperature operations.

1.2.1 Titanium alloy grades

In the aerospace and military industries, six distinct forms of pure titanium and four distinct titanium alloys are used. Pure titanium comes in a variety of grades, including CP4 (Grade 1), CP3 (Grade 2), CP2 (Grade 3), CPI (Grade 4), Titanium (Grade 7), and CP Ti-0.15Pd (Grade 11). There are four different grades of titanium alloy available, including Grade 5 Ti-6Al-4V, Grade 6 Ti-5Al-2.5Sn, Grade 12 Ti-3Al-2.5, and Grade 23 Ti-6AL-4V ELI. For high-strength castings and other industrial applications, the most common titanium alloy is Ti-6Al-4V. Over half of the global market is now dominated by this material because of its superior strength-to-density ratio, less weight, increased use at high temperatures, resistance to corrosion, and galvanic compatibility. Although phase distribution, microstructure, and final heat treatment conditions have a significant impact on mechanical strength, corrosion resistance, and high-temperature application in Ti-6Al-4V alloys, these properties are not independent of one another. When a material is heated or cooled beyond the -transus temperature, it transforms into a coarse grain lamellar microstructure, while a fine equiaxed (globular) microstructure remains unchanged. Coarse grain lamellar improves crack formation and creep characteristics at the expense of ductility and fatigue resistance. Bimodal structures, because of their balanced phase distribution, may exhibit fatigue, creep behaviour, and ductility (Sieniawski et al., 1997; Liitjering, 1998).

1.2.2 Titanium powder

Titanium alloy powder is the fundamental ingredient in the Laser Powder Bed Fusion (LPBF) technique, which employs gas atomization techniques to produce finely alloyed powders. Additive manufacturing, powder sintering, electron beam melting, selective laser melting, and metal injection moulding are all viable options when working with these powders. However, the varying particle sizes that might result from atomization methods provide difficulties in powder feed applications. With the right approach, powdered substances may be evenly distributed in size.

1.3 Laser Powder bed fusion (LPBF) processes

Thijs et al. (2010) and Simonelli et al. (2014) both agree that the Laser Powder Bed Fusion (LPBF) process is a fast and effective method for creating complex geometries. The procedure entails heating the part-construction platform, dispersing metal powder, melting the powder under control, and finally cooling the metal. The outcome is a microstructure of previous grains characterised by metastable a'-martensite. Harmonious microstructures in Ti-6Al-4V alloy may be achieved with careful adjustment of process parameters, leading to improved performance in harsh environments. Increased mechanical properties are achieved by the development of the harder a'-martensite phase and the elongation of martensite grains through partial re-melting. The microstructure, ductility, fatigue, and phase distribution properties of Ti-6Al-4V alloy may be drastically altered by the LPBF method.*Part Manufacturing:* The primary goal of part manufacturing utilizing the LPBF technological advances is to transform digital information into a geometric entity possessing mechanical attributes that are akin to those achieved through conventional manufacturing methodologies.

- *Parameter Optimization:* This study introduces a methodology that aims to optimize process parameters in order to attain enhanced rigidity. The approach employed is based on a general factorial framework and incorporates the principles of decision-making based on multiple criteria.
- *Post-process:* The process of preparing the specimen involves subsequent treatment procedures, such as heat treatment and annealing, which are implemented to mitigate the formation of a'-martensite.

1.4 Techniques for Material Characterization

- *FE-SEM:* FESEM employs cutting-edge imaging technology to conduct a thorough evaluation of specimens in surface-sensitive and non-conductive materials. This technique allows for the attainment of ultra-high resolution and unparalleled contrast in the realm of metallurgical research.
- *XRD:* It serves to ascertain the structural composition, lattice dimensions, mechanical stress, and inherent imperfections within crystalline entities, thereby discerning their amorphous or crystalline nature.
- *XPS: XPS* is a technique using Al Ka X-rays to analyse a material's surface. An electron energy analyser helps determine elemental composition, chemical configuration, and species abundance by analysing photoelectrons' binding power and intensity, providing valuable insights into properties.
- *STM:* STM effectively reveals surface topography and detects defects.

2. LITERATURE REVIEW

This section explores the study of mechanical properties, microstructure, phase transformation characteristics, heat treatment, and stress-strain rate testing in LPBF titanium alloy, focusing on corrosion properties to enhance our understanding of this subject matter.

2.1 The additive manufacturing process (AM)

Sun et al. (2017) conducted a comprehensive analysis of the additive manufacturing (AM) technique using LPBF, focusing on its unique attributes, processing parameters, melt pool intricacies, microstructural properties, residual stresses, cracking, distortion, defects, and density. Emmelmann et al. (2017) explored the design autonomy of AM, focusing on the use of laser beams for melting and solidification of materials. Brandt (2017) highlighted the use of CO2 lasers, flash lamps, and diode-pumped neodymium-doped yttrium-aluminum-garnet (Nd: YAG) lasers, which have an efficiency range of 30-40%. Leary (2017b) investigated various orientation techniques to enhance surface finish of components produced through LPBF, examining the staircase effect, powder particle adhesion, and surface roughness.

Liu et al. (2017) explored additive manufacturing in the aerospace sector, highlighting its advantages in streamlining production processes and providing architectural flexibility and assembly interactions. Munsch (2017) examined AM in personalized medical implants, categorizing biocompatible materials into polymeric and metallic categories based on their biocompatibility and characteristics. Al-Ketan et al. (2018) examined lattice-structured unit cellular designs using Selective Laser Melting (SLM) techniques, revealing superior mechanical performance and robustness. Yuan and Gu (2015) used a three-dimensional finite-volume methodology to investigate the thermal evolution of solid-liquid pyrolysis (SLM) and found that Marangoni convection affects mass and heat transport. The melting pool geometry showed a positive correlation with laser power increase and a negative correlation with scan speed variation. The laser source in motion exhibited a Gaussian distribution, indicating nonlinearity due to temperature-dependent material characteristics.

2.2 Additive manufacturing of Ti-6Al-4V alloy

Khorasani et al. (2019) studied the mechanical properties of Ti-6Al-4V alloy fabricated through selective laser melting (SLM) using the Taguchi design experiment approach. They analyzed the influence of process parameters on material properties, including microhardness, tensile strength, and density. They also analysed hatch space, scan speed, heat treatment, and laser-pattern angle procedure. Wang et al. (2019) focused on surface density and roughness characteristics, achieving mechanical strength comparable to commercial titanium alloys. The study focused on the formation of microstructure, specifically a'-martensite, and heat treatment effects. Levkulich et al. (2019) examined the impact of process parameters on residual stress in Ti-6Al-4V alloy fabricated using SLM technology. They found that laser melting induces rapid cooling rates and significant temperature gradients, resulting in substantial residual stress and deformation. Various techniques were used to analyse stress, including hole drilling, x-ray diffraction, laser line profilometry, and contour method. Integrating non-destructive methods can enhance understanding of the impact of process variables on residual distortion and stress levels. Zhang et al. (2019) found that incorporating copper into Ti-6Al-4V alloy reduced high-temperature gradients in laser powder melting processes, resulting in fine-grained and equiaxed specimens. He et al. (2019) evaluated the geometry and microstructure of Ti-6Al-4V alloy melt pools using a powder-free technique, incorporating boron within a 1-10% percentage range. This method provided valuable insights into the melt pool's behavior during powder incorporation. Ghouse et al. (2017) investigated manufacturing techniques and materials in powder bed fusion, focusing on high cycle fatigue strength and compressive strength of porous materials. Todaro et al. (2020) used high-intensity ultrasound to achieve equiaxed grain structure in Ti-6Al-4V alloy, enhancing tensile strength and yield stress by 12%. This advancement has facilitated its adoption in high-capacity settings, resulting in enhanced mechanical characteristics. Barriobero-Vila and Sheydaeian (2017) used heat treatment techniques to improve the mechanical strength of Ti-6Al-4V alloy during selective laser melting. They optimized porosity levels and observed martensitic decomposition, leading to a refined lamellar a+ microstructure. Khorasani et al. (2019) found that decreased laser strengths, pattern angles, and scan speeds improved density outcomes. Todd et al. (2019) used resonant ultrasound measurements to forecast mechanical properties, revealing more accurate predictions for yield strength, ultimate tensile strength, and Young's modulus. Mahdavi et al. (2020) found a correlation between AM process parameters and MTS parameters, and enhanced process models by incorporating laser power and scan speed. Sokolov et al. (2020) examined the effects of hot rolling treatments on Ti-6Al-4V alloy, revealing significant structural changes, elimination of porosity, and enhanced mechanical properties.

2.3 Microstructure and thermal treatment of Ti-6Al-4V alloy additive.

Khorasani et al. (2019) optimized LPBF processes using the Design of Experiments (DOE) technique. They created 125 specimens and examined the effects of scan speed, laser power, laser pattern angle, hatch spacing, and thermal treatment on construction and production processes. Laser power was the most important building parameter, followed by thermal treatment, scan speed, laser pattern angle, and hatch spacing. Lee et al. (2017) improved thermal treatment parameters using the Taguchi technique, examining the impact of fan, duration, solution temperature, quench delay time, protective gas, temperature, cooling rate, and aging treatment duration on quality features like microhardness, aging, and tensile strength. The temperature of aging had the greatest effect on post-aging firmness. Wang et al. (2016) investigated surface modification of heat-treated Ti-6Al-4V alloy, uncovering surface modifications, roughness, morphology, mechanical properties, and crystalline structure. Markovsky and Semiatin (2011) found that local swift heat treatment significantly improved lamellar microstructure compared to equiaxed microstructure. Raghavan et al. (2018) investigated the effect of thermal treatment on mechanical and microstructure properties of Ti-6Al-4V alloy using various techniques, revealing that solution air-cooled and aged specimens had improved tensile properties and a+ morphology refinement.

2.4 AM of Ti-6Al-4V alloy

Micromechanical and dynamic tensile characteristics of Ti-6Al-4V alloy sheet were studied by Zhou et al. (2019) at high strain rates. The specimens were reproduced three times and sectioned in a variety of orientations. Ductile fracture was evident in the Ti-6Al-4V alloy sheet, as shown by the dimple-shaped voids and anisotropic properties. The vulnerability of Ti-6Al-4V alloy to hydrogen embrittlement was investigated by Koide et al. (2017). There was no change in elongation or decrease in area at the fractured surfaces, indicating that the failure was ductile. Stress corrosion cracking (SCC) in a Ti-6Al-4V alloy was studied by Liu et al. (2020) in a 3.5% sodium chloride solution at hydrostatic pressure. The presence of hydrides and stress corrosion cracking were shown to cause hydrogen embrittlement at the contact. In addition to increasing the flexibility of Ti-6Al-4V alloy during laser cladding, the presence of the a-P interface phase was found by Zhao et al. (2017) to limit dislocation motion and generate deformed twins. Dynamic straining in stress corrosion cracking and the slow strain rate test (SSRT) were the focus of Henhorne's (2016) research. The sensitivity of P-annealed Ti64 alloy to stress corrosion cracking in an aqueous solution containing 0.6 M NaCl was studied by Jeong et al. (2018) using a slow strain rate test to examine the effect of applied potentials. The material's resistance to SCC was significantly improved by raising the intermediate fracture fraction. Stabilising annealing was shown to reduce Ti64 alloy's susceptibility to hydrogen-induced SCC.

3. MATERIAL AND METHODS

3.1 The properties of the base material

An element with allotropy, such as titanium, can take on several crystallographic forms. When exposed to temperatures exceeding 995°C, the material transitions into a body-centered cubic (beta- α) phase from the material's room temperature hexagonal close-packed (alpha- β) phase (Vrancken et al., 2012). The goal of alloying is phase stability, where the coexistence of the β phase and α phase at room temperature is made possible by suitable additions. Three separate classes of titanium alloys can be distinguished according to where they fall on a quasi-binary section. These categories are identified by the symbols α, β, and α+β. The presence of a bi-modal " α+β " microstructure gives the titanium alloy outstanding mechanical properties. These qualities include exceptional strength, decreased weight, corrosion resistance, and appropriateness for usage in high-temperature settings.

Table 1: Grade mechanical properties of alloy Ti-6Al-4V

Ultimate tensile strength (MPa)	Yield Stress (MPa)	% Elongation	Micro hardness (HV)
950	880	14	349

3.2 Designing of the experiment

The study aimed to create a structure without porosity using the 3-factor-3 level method, involving manipulation of scan speed, laser power, and scan offset distance. A total 27 parameter sets were used, following the Department of Energy's procedures and the Taguchi general full factor design method. The parameters ranged from 270 W to 310 W for power, 1280 mm/s to 340 mm/s for speed, and 0.09 mm to 0.15 mm for scan offset distance. Wang et al. (2019) found that a laser power exceeding 230 W and a scan speed exceeding 1150 mm/s were the most optimal combination for achieving a structure devoid of porosity. The L 27 array was used for the experiment, with process parameters (Table 2) including scan speeds (1280, 1310, 1340), offset distances (0.09, 0.12, and 0.15 mm), and laser powers (270, 290, 310).

Table 2: LPBF processing parameters: Laser power, scan rate, offset distance, and data levels.

Laser power (W)	Laser scan speed (mm/s)	Scan offset distance (mm)
950	1280	0.09
290	1310	0.12
310	1340	0.15

Laser energy density calculation using equation 1 considers factors like P-laser power, Ev-volumetric energy density, hatch spacing, layer thickness, and scan speed. Ion et al. (1992) found energy density more precise in volume constructs compared to 2D surfaces.

$$Ev = P/ (v \, . \, h \, . \, t) \ J/mm^3 \quad (1)$$

3.2.1 Characterization of Ti-6Al-4V powder.

Table 3: Ti-6Al-4V powder chemical composition

Elemental composition (wt.%)									
Elements	Al	V	0	N	C	Fe	Yb	Other	Ti
Percentage weight (wt.%)	5.5-6.75	3.5-4.5	0.2	0.05	0.08	0.3	0.005	0.515	Balance

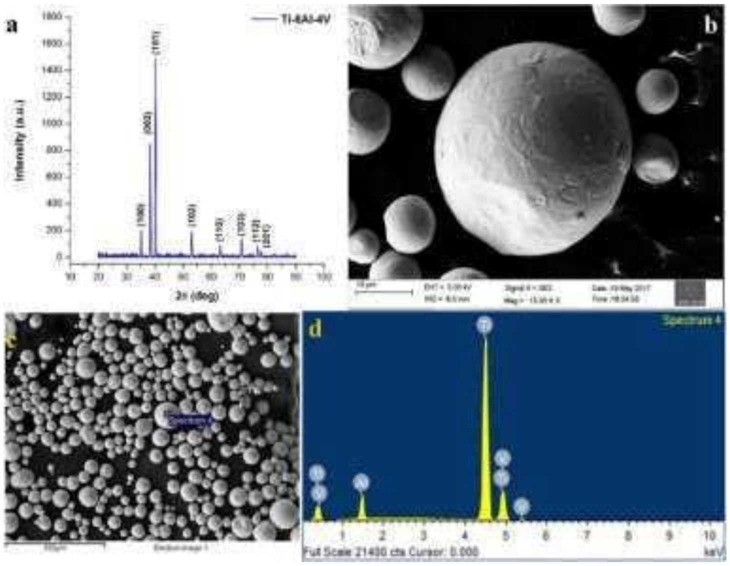

Figure 1 (a-d): (a) X-ray diffraction pattern, (b-c) surface morphology, and (d) EDAX profile of Ti-6Al-4V powder.

3.2.2 Heat treatment of the alloy Ti-6Al-4V

The L27 and L9 orthogonal arrays underwent heat treatment, 850°C exposure, argon cooling, shot peening, cleaning, and wire-cut electro-discharge machining to eliminate surface contaminants and roughness (Figure 2). Analytical techniques like FESEM, XRD, XPS, and STM were used to characterize the samples, along with mechanical tests like tensile testing, microhardness assessment, and corrosion analysis. The L27 sample and build platform were also subjected to immediate heat treatment.

Figure 2 (a, b): Furnace and Shot peening

3.2.3 XRD-based characterisation

The Ti-6Al-4V alloy underwent XRD research to examine phase transition characteristics and the effects of heat treatment on residual stress generation and annealing. Results from the L9 and L27 studies were assessed.

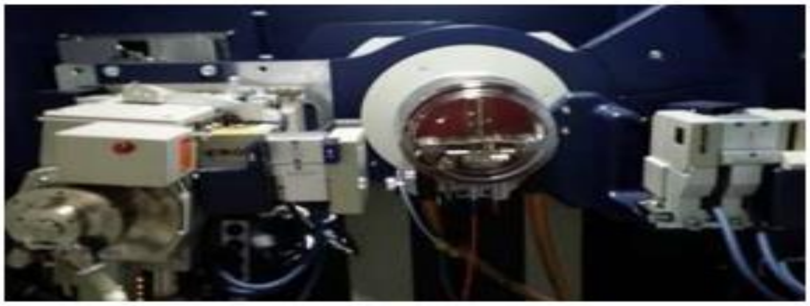

Figure 3: XRD

3.2.4 FESEM Characterization

The study analysed the microstructure of a selected specimen from orthogonal L27 specimens using an optimization technique considering mechanical characteristics and processing parameters. The specimen was examined using a Field Emission Scanning Electron Microscope (FE-SEM) (Figure 4) and fractography was documented at multiple magnification levels. Prior to high-resolution scanning, the specimens underwent preparatory steps, including polishing, cleaning, and sonication. FE-SEM uses a high-energy electron beam to produce visual representations of the specimen's surface, generating signals about topographical features, chemical composition, and other characteristics. The main difference between SEM and FESEM lies in the emitter type. The detector captures secondary electrons, generating an electrical signal that can be displayed on a computer screen or preserved for analysis and manipulation.

Figure 4: FESEM

3.2.5 STM Characterization

The scanning tunneling microscope (STM) was utilized to conduct the analysis on a DOE L27 optimized specimen. The investigation focused on the topography and transition from a'-martensite to a+ lamellar structure, as shown in Figure 5a. The specimens underwent a two-step heating process, starting with an initial heating to 70°C, followed by subsequent heating to 800°C. After reaching the desired temperature, the specimens were maintained at this level for a duration of 90 minutes. Prior to being introduced into the STM chamber, the specimens underwent a polishing and cleaning procedure. This entire process is illustrated in Figure 5 (b). In situ, thermal treatment and analysis were conducted using a customized specimen holder, as depicted in Figure 5 (c) and (d). The manuscript discusses the crystallographic pattern observed through the use of STM measurements.

Figure 5 (a-d): (a) STM (b) Heating chamber (c) Study utilizes AM with Ti-6Al-4V for fabricating specimen holder and specimen. (d) Heat-treated specimen with holder.

3.2.6 Tensile strength test

Tensile tests were performed on specimens in accordance with the ASTM E8M standard, utilizing the BISS (P) LTD-India, UT-01-0025 equipment as depicted in Figure 6. Tensile experiments were conducted on a set of 27 specimens denoted as L, which were specifically designed by manipulating scan offset distance, scan speed, and laser power variables. A plot was generated to examine the correlation between percentage elongation and stress, revealing that fractures took place at the midpoint of the gauge length.

Figure 6:(a) Tensile test machine (b) Specimen with holder clamp

The experiment measured tensile test values at two yield points: 0.2 mm offset yield point and breaking point for ultimate tensile strength.

3.2.7 Microhardness and Density test

The relative density of Ti-6Al-4V alloy samples was the primary focus of the study.

3.2.8 Analysis of Weight loss

The weight loss of a piece of heat-treated Ti-6Al-4V when submerged in a NaCl solution was studied. The areas to be treated were cleaned and measured before any work was done. The specimen was treated with a solution of the combination for a total of 72 hours.*XPS analysis*

The XPS method is used for surface analysis of many different types of materials. Spectroscopy analysis was used to determine the concentrations of Ti, Al, and V in the samples both before and after they were treated with NaCl solution. After etching the specimens with a 0.1 m etchant, survey spectra were also obtained.

3.2.9 Corrosion test

Using the LPBF method, electrochemical studies were performed on 8x8x4 mm Ti-6Al-4V specimens. Process parameter optimisation was used to make the call. Epoxy resin was cold-embedded in both non-heat-treated and heat-treated specimens, and both sets of specimens were cured at room temperature. Using SiC diamond paste and emery sheets, the surface roughness of the metal was reduced by 0.3 microns during the polishing process. To remove contaminants, ultrasonic cleaning in an ethanol-water solution was performed on the specimens. The experimental setup for assessing corrosion is shoFigure 7.

Figure 7: Corrosion test equipment

4. RESULTS AND DISCUSSION

4.1 Mechanical properties

A. Tensile examination of specimen according to L9 orthogonal array

Tensile tests were conducted on nine specimens using a BISS tester, with layer thickness and hatch distance set at 0.04mm and 0.15mm. The ASTM E8M standard guidelines were followed, and measurements were taken to record stress-elongation relationship. The samples with a scan speed of 1340 mm/sec and 310 W achieved the highest elongation percentage of 10.88% and tensile strength of 1040 MPa.

Table 4: Ti-6Al-4V's elongation, tensile strength, laser power, density, scan speed.

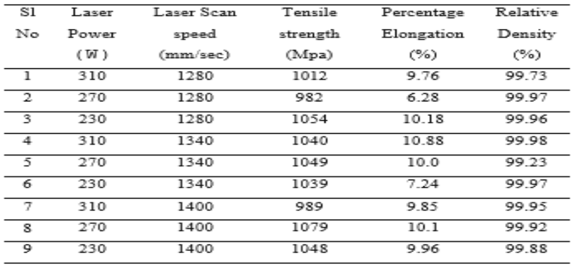

Sl No	Laser Power (W)	Laser Scan speed (mm/sec)	Tensile strength (Mpa)	Percentage Elongation (%)	Relative Density (%)
1	310	1280	1012	9.76	99.73
2	270	1280	982	6.28	99.97
3	230	1280	1054	10.18	99.96
4	310	1340	1040	10.88	99.98
5	270	1340	1049	10.0	99.23
6	230	1340	1039	7.24	99.97
7	310	1400	989	9.85	99.95
8	270	1400	1079	10.1	99.92
9	230	1400	1048	9.96	99.88

B. Micro-hardness and Density of L9 specimen

Ti-6Al-4V samples were weighed, and the laser-printed one was found to have a higher density (99.98%) than the rest. A Vickers hardness test was used to measure the microhardness of the final, optimized sample. L9 performed the best out of the three tested parameters (412 HV, 376 HV, and 389 HV). The optimal testing range was increased to L27 by integrating L9's optimal parameters.

C. Results of TOPSIS DOE L27

The optimization of the LPBF process parameters was accomplished through the utilization of TOPSIS, an approach for multi-criteria decision-making. The outcomes of ultimate tensile strength, tensile strength tests, and elongation for 27 samples are presented in Table 5. The data underwent evaluation using the TOPSIS method, resulting in the identification of the most suitable specimens. The objective was to identify a singular index-based solution for assessing the impact of LPBF process variables on mechanical characteristics. Equal weightage was assigned to elongation, microhardness, and tensile strength, and closeness values were subsequently calculated and placed in accordance.

Table 5: L27 laser constraints distribution, relative density, energy density, elongation, tensile strength, microhardness.

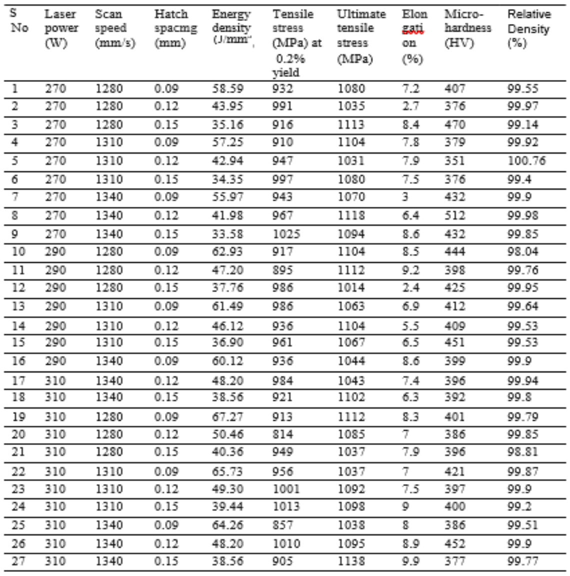

S No	Laser power (W)	Scan speed (mm/s)	Hatch spacmg (mm)	Energy density (J/mm^3	Tensile stress (MPa) at 0.2% yield	Ultimate tensile stress (MPa)	Elongation (%)	Micro-hardness (HV)	Relative Density (%)
1	270	1280	0.09	58.59	932	1080	7.2	407	99.55
2	270	1280	0.12	43.95	991	1035	2.7	376	99.97
3	270	1280	0.15	35.16	916	1113	8.4	470	99.14
4	270	1310	0.09	57.25	910	1104	7.8	379	99.92
5	270	1310	0.12	42.94	947	1031	7.9	351	100.76
6	270	1310	0.15	34.35	997	1080	7.5	376	99.4
7	270	1340	0.09	55.97	943	1070	3	432	99.9
8	270	1340	0.12	41.98	967	1118	6.4	512	99.98
9	270	1340	0.15	33.58	1025	1094	8.6	432	99.85
10	290	1280	0.09	62.93	917	1104	8.5	444	98.04
11	290	1280	0.12	47.20	895	1112	9.2	398	99.76
12	290	1280	0.15	37.76	986	1014	2.4	425	99.95
13	290	1310	0.09	61.49	986	1063	6.9	412	99.64
14	290	1310	0.12	46.12	936	1104	5.5	409	99.53
15	290	1310	0.15	36.90	961	1067	6.5	451	99.53
16	290	1340	0.09	60.12	936	1044	8.6	399	99.9
17	310	1340	0.12	48.20	984	1043	7.4	396	99.94
18	310	1340	0.15	38.56	921	1102	6.3	392	99.8
19	310	1280	0.09	67.27	913	1112	8.3	401	99.79
20	310	1280	0.12	50.46	814	1085	7	386	99.85
21	310	1280	0.15	40.36	949	1037	7.9	396	98.81
22	310	1310	0.09	65.73	956	1037	7	421	99.87
23	310	1310	0.12	49.30	1001	1092	7.5	397	99.9
24	310	1310	0.15	39.44	1013	1098	9	400	99.2
25	310	1340	0.09	64.26	857	1038	8	386	99.51
26	310	1340	0.12	48.20	1010	1095	8.9	452	99.9
27	310	1340	0.15	38.56	905	1138	9.9	377	99.77

The computation of the normalized matrix for microhardness, elongation, and tensile stress is presented in Table 4.3. The process of calculating the weighted normalizing matrix was performed for each column using a weight value of 0.33. The resulting values were then recorded in Table 7.

Table 6: Calculation of Normalized matrix

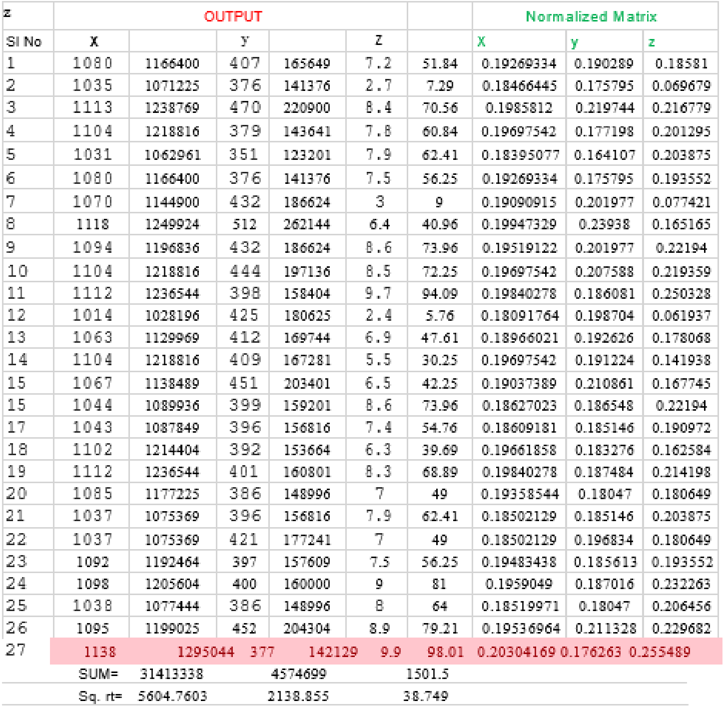

z	OUTPUT						Normalized Matrix		
Sl No	x		y		z		x	y	z
1	1080	1166400	407	165649	7.2	51.84	0.19269334	0.190289	0.18581
2	1035	1071225	376	141376	2.7	7.29	0.18466445	0.175795	0.069679
3	1113	1238769	470	220900	8.4	70.56	0.1985812	0.219744	0.216779
4	1104	1218816	379	143641	7.8	60.84	0.19697542	0.177198	0.201295
5	1031	1062961	351	123201	7.9	62.41	0.18395077	0.164107	0.203875
6	1080	1166400	376	141376	7.5	56.25	0.19269334	0.175795	0.193552
7	1070	1144900	432	186624	3	9	0.19090915	0.201977	0.077421
8	1118	1249924	512	262144	6.4	40.96	0.19947329	0.23938	0.165165
9	1094	1196836	432	186624	8.6	73.96	0.19519122	0.201977	0.22194
10	1104	1218816	444	197136	8.5	72.25	0.19697542	0.207588	0.219359
11	1112	1236544	398	158404	9.7	94.09	0.19840278	0.186081	0.250328
12	1014	1028196	425	180625	2.4	5.76	0.18091764	0.198704	0.061937
13	1063	1129969	412	169744	6.9	47.61	0.18966021	0.192626	0.178068
14	1104	1218816	409	167281	5.5	30.25	0.19697542	0.191224	0.141938
15	1067	1138489	451	203401	6.5	42.25	0.19037389	0.210861	0.167745
15	1044	1089936	399	159201	8.6	73.96	0.18627023	0.186548	0.22194
17	1043	1087849	396	156816	7.4	54.76	0.18609181	0.185146	0.190972
18	1102	1214404	392	153664	6.3	39.69	0.19661858	0.183276	0.162584
19	1112	1236544	401	160801	8.3	68.89	0.19840278	0.187484	0.214198
20	1085	1177225	386	148996	7	49	0.19358544	0.18047	0.180649
21	1037	1075369	396	156816	7.9	62.41	0.18502129	0.185146	0.203875
22	1037	1075369	421	177241	7	49	0.18502129	0.196834	0.180649
23	1092	1192464	397	157609	7.5	56.25	0.19483438	0.185613	0.193552
24	1098	1205604	400	160000	9	81	0.1959049	0.187016	0.232263
25	1038	1077444	386	148996	8	64	0.18519971	0.18047	0.206456
26	1095	1199025	452	204304	8.9	79.21	0.19536964	0.211328	0.229682
27	1138	1295044	377	142129	9.9	98.01	0.20304169	0.176263	0.255489
	SUM=	31413338		4574699		1501.5			
	Sq. rt=	5604.7603		2138.855		38.749			

Table 7: Normalized matrix calculation

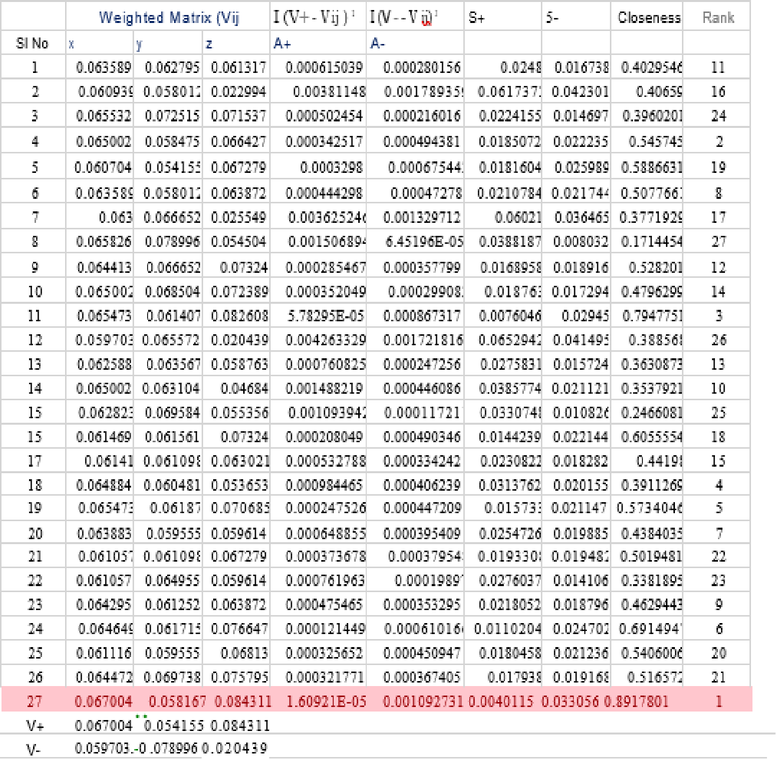

	Weighted Matrix (Vij			I (V+ - Vij)²	I (V - - V ij)²	S+	5-	Closeness	Rank
Sl No	x	y	z	A+	A-				
1	0.063589	0.062795	0.061317	0.000615039	0.000280156	0.0248	0.016738	0.4029546	11
2	0.060939	0.058012	0.022994	0.00381148	0.001789359	0.0617371	0.042301	0.40659	16
3	0.065532	0.072515	0.071537	0.000502454	0.000216016	0.0224155	0.014697	0.3960201	24
4	0.065002	0.058475	0.066427	0.000342517	0.000494381	0.0185072	0.022235	0.545745	2
5	0.060704	0.054155	0.067279	0.0003298	0.000675441	0.0181604	0.025989	0.5886631	19
6	0.063589	0.058012	0.063872	0.000444298	0.00047278	0.0210784	0.021744	0.5077661	8
7	0.063	0.066652	0.025549	0.003625246	0.001329712	0.06021	0.036465	0.3771929	17
8	0.065826	0.078996	0.054504	0.001506894	6.45196E-05	0.0388187	0.008032	0.1714454	27
9	0.064413	0.066652	0.07324	0.000285467	0.000357799	0.0168958	0.018916	0.528201	12
10	0.065002	0.068504	0.072389	0.000352049	0.000299081	0.018763	0.017294	0.4796299	14
11	0.065473	0.061407	0.082608	5.78295E-05	0.000867317	0.0076046	0.02945	0.7947751	3
12	0.059703	0.065572	0.020439	0.004263329	0.001721816	0.0652942	0.041495	0.388568	26
13	0.062588	0.063567	0.058763	0.000760825	0.000247256	0.0275831	0.015724	0.3630873	13
14	0.065002	0.063104	0.04684	0.001488219	0.000446086	0.0385774	0.021121	0.3537921	10
15	0.062823	0.069584	0.055356	0.001093942	0.00011721	0.0330748	0.010826	0.2466081	25
15	0.061469	0.061561	0.07324	0.000208049	0.000490346	0.0144239	0.022144	0.6055554	18
17	0.06141	0.061098	0.063021	0.000532788	0.000334242	0.0230822	0.018282	0.44195	15
18	0.064884	0.060481	0.053653	0.000984465	0.000406239	0.0313762	0.020155	0.3911269	4
19	0.065473	0.06187	0.070685	0.000247526	0.000447209	0.015733	0.021147	0.5734046	5
20	0.063883	0.059555	0.059614	0.000648855	0.000395409	0.0254726	0.019885	0.4384035	7
21	0.061057	0.061098	0.067279	0.000373678	0.00037954	0.019330	0.019482	0.5019481	22
22	0.061057	0.064955	0.059614	0.000761963	0.00019897	0.0276037	0.014106	0.3381895	23
23	0.064295	0.061252	0.063872	0.000475465	0.000353295	0.0218052	0.018796	0.4629443	9
24	0.064649	0.061715	0.076647	0.000121449	0.000610166	0.0110204	0.024702	0.6914947	6
25	0.061116	0.059555	0.06813	0.000325652	0.000450947	0.0180458	0.021236	0.5406006	20
26	0.064472	0.069738	0.075795	0.000321771	0.000367405	0.017938	0.019168	0.516572	21
27	0.067004	0.058167	0.084311	1.60921E-05	0.001092731	0.0040115	0.033056	0.8917801	1
V+	0.067004	0.054155	0.084311						
V-	0.059703.	-0 .078996	0.020439						

The response table provides a predictive model for determining the sequence in which mechanical characteristics affect the specimens listed in Table 8.

Table 8: Response variable

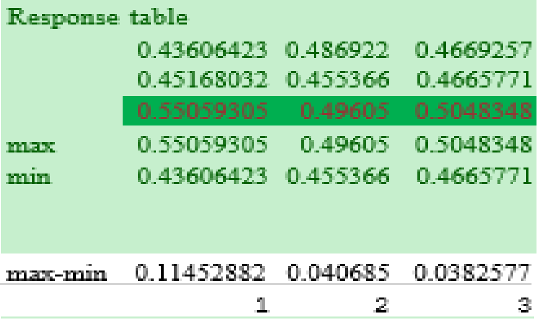

Response table			
	0.43606423	0.486922	0.4669257
	0.45168032	0.455366	0.4665771
	0.55059305	0.49605	0.5048348
max	0.55059305	0.49605	0.5048348
min	0.43606423	0.455366	0.4665771
max-min	0.11452882	0.040685	0.0382577
	1	2	3

The TOPSIS analysis revealed that specimen No. 27, which was subjected to a scan speed of 1340, a hatch spacing of 0.15 mm, and a laser power of 310 W exhibited the highest level of efficiency in terms of its mechanical properties. The strength of the material was found to be significantly affected by the laser power, with hatch spacing and scan speed also playing a notable role.

D. Tensile strength Results

The experimental findings indicate a direct correlation between energy density and the tensile strength of the material. According to Belle et al. (2013), the volumetric energy density exhibits a distribution within the range of 37.6-67.3 J/mm3, leading to a melt zone temperature exceeding 3000°C. A total of three specimens (as indicated in Table 5) exhibited elongation values equal to or exceeding 9%: specifically, specimens No. 11 (9.2%), No. 24 (9.9%), and No. 27 (9.9%). The experiment involved the utilization of laser powers of 270 W and 290 W to measure elongation. The observed elongation values were 2.7%, 3%, and 2.4% respectively. In contrast, the use of a laser power of 310 W consistently resulted in high elongation, reaching a maximum value of 9.9%. This finding suggests that the utilization of a 310 W laser power consistently results in a significant increase in elongation, irrespective of the specific values assigned to scan speed and hatch spacing parameters.

E. Results of Microhardness

Several specimens showed microhardness values ranging from 350 to 380 HV, similar to those in wrought Ti-6Al-4V alloy. Three specimens had low elongation, while two had high elongation. Microhardness showed no significant variation. Microstructure showed variations in plasticity and yield stress, while microhardness correlated with surface texture. Tensile performance was correlated with internal and surface texture characteristics. Optimization of microhardness and tensile strength produced a specimen with a tensile stress of 1138 MPa, microhardness of 377 HV, and elongation of 9.9%. The specimen underwent optimization and underwent microstructure analysis using XRD, FE-SEM, and STM.

4.2 Microstructure of AM Ti-6Al-4V alloy

A. XRD result analysis

The X-ray diffraction (XRD) patterns of non-heat-treated and heat-treated Ti-6Al-4V alloys, produced using the Selective Laser Melting (LPBF) technique, are depicted in Figure 8. The heat-treated specimens exhibit the highest peaks for the body-centered cubic framework. The lattice parameters were determined through the analysis of XRD patterns, as described by Frentrup et al. (2013). It was observed that the values for the lattice parameters "a" and "c" were distinct between the non-high-temperature (non-HT) and high-temperature (HT) specimens. The specimens subjected to HT conditions exhibited values of 4.6684 ± 0.0014 A and 2.9381 ± 0.0016 A, whereas the non-HT specimens displayed values of 4.6593 ± 0.0020 A and 2.9235 ± 0.0012 A. The c/a ratio of the high-temperature (HT) specimens was measured to be 1.589 A, whereas the non-high-temperature (non-HT) specimens exhibited a slightly higher ratio of 1.593 A.

B. FE-SEM result analysis

The microstructure of the specimen depicted in Figure 9 (a) and (b) exhibits the presence of coarse grains and micro voids characterized by a curvilinear profile. Grain pockets of larger size exhibit a curvilinear morphology, whereas pockets of smaller size possess a boundary that accommodates smaller grains. The presence of microcavities was observed as a result of the distribution of built layers and the occurrence of keyhole effects.

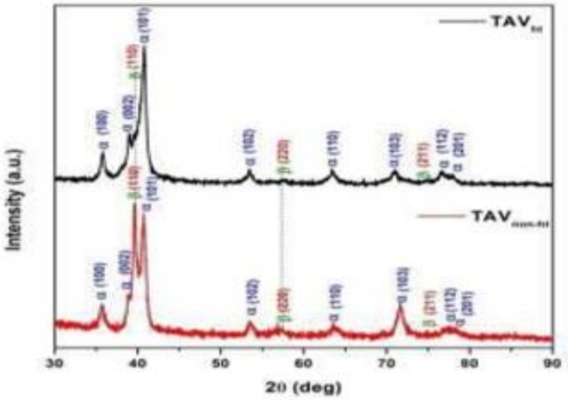

Figure 8: X-ray diffraction patterns for Ti-6Al-4V alloy generated by the LPBF method under heat treatment and non-heated conditions.

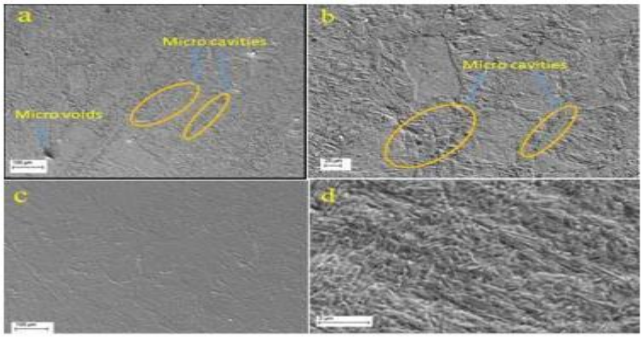

Figure 9 (a) The microstructure of the printed specimen was observed at a magnification of 1000X, with a resolution of 100 µm. (b) at 20 µm and 2.5 Kx resolution (c) The microstructure of the heat-treated specimen was observed at a magnification of 1000X, with a resolution of 100 µm. (d) Magnification of resolution and 76 Kx 2 µm

Figure 10 (a-d) illustrates the contrasting microstructural characteristics observed in Ti-6Al-4V specimens subjected to heat treatment and those that were not. The primary phase observed is a'-martensite, accompanied by the presence of both a and β distributions. Figure 11 exhibits the microstructure of specimens made from Ti-6Al-4V, showcasing both unheated and heat-treated samples at higher levels of magnification. The present study demonstrates the generation of a similar morphology through the utilization of high-speed laser scanning rates. This approach allows for the visualization of a well-developed neurostructural feature, as depicted in Figure 12.

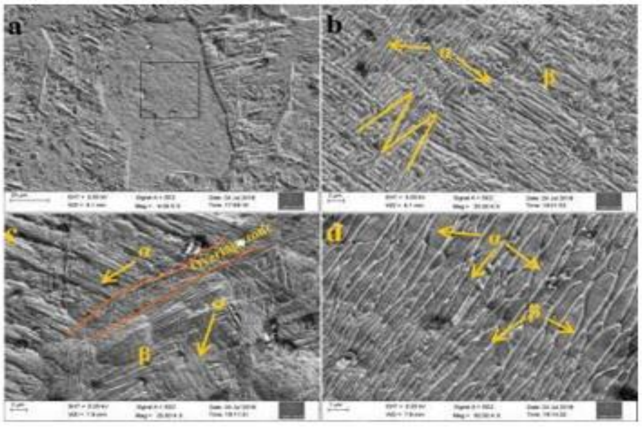

Figure 10 (a-d): Microstructure of printed Ti-6Al-4V specimens made using the LPBF technique (a & b) and heat-treated (c & d).

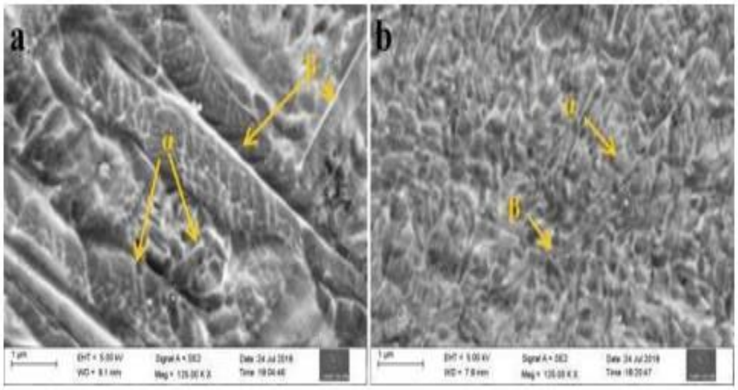

Figure 11: FESEM images of (a) non-heat treated and (b) heat-treated Ti-6Al-4V samples

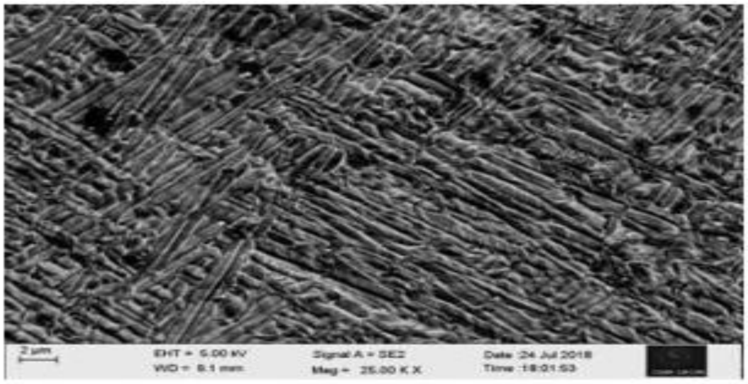

Figure 12: Ti-6Al-4V alloy microstructure resulted from higher laser scan rates for a 3D-printed part

4.2.3 Microstructure impact on the mechanical characteristics of Ti-6Al-4V alloy processed by LPBF

A lamellar/equiaxed a+ architecture is suggested for the specimen microstructure in order to improve its mechanical characteristics. Figure 13 illustrates how the microstructure of the specimen is affected by the carefully controlled furnace heat treatment necessary for lamellar/equiaxed a+ production.

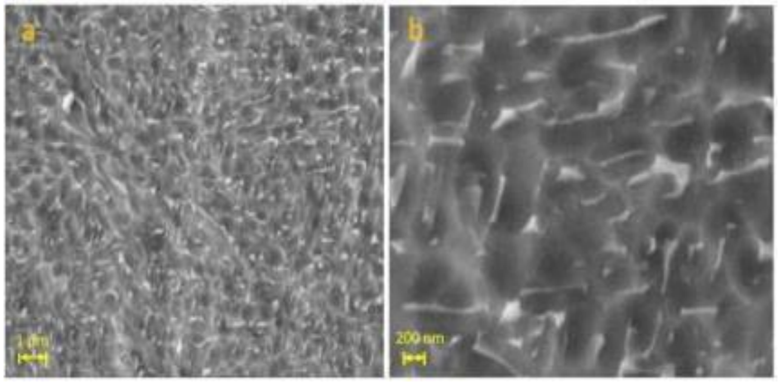

Figure 13a: Specimen for Microstructure (a) exceeding 10% in elongation at μm resolution; Scan speed 1340 mm/sec, Laser power 310 W, and 0.15 mm Hatch distance (b) at higher resolution 200 nm.

According to Table 5, there are three specimens exhibiting elongation values of 9% and higher. Notably, specimen No. 27 is distinguished by the presence of a conformal β precipitation. The influence of βaggregates on its elongation property and the efficiency of the a+β bi-model framework is observed. The observed enhancement in elongation and tensile strength can be ascribed to the influence of grain size, as depicted in Figure 13b (Xu et al., 2015). Certain specimens that were subjected to a laser power of 270 W exhibited a limited degree of elongation, whereas specimens treated with a laser power of 310 W consistently maintained an elongation value exceeding 6.3%.

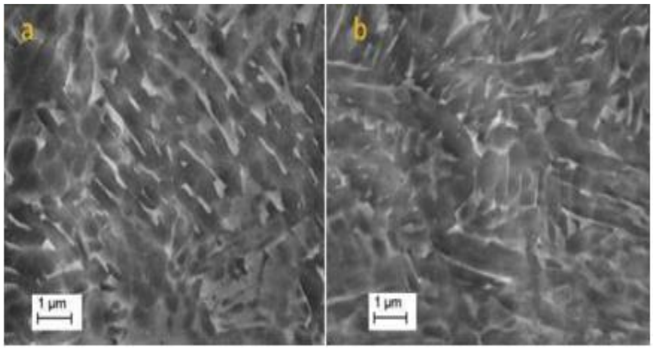

Figure 13b: Microstructures of (a) sample 24 with 9% elongation; and (b) sample 11 with 9.2% elongation

4.2.4 Machining Effect on tensile performance

The tensile strength of specimens is influenced by the surface morphology, wherein the presence of surface features plays a significant role in determining performance outcomes. The conducted tensile tests on specimen No. 27 (with a width of 310 W, a loading rate of 1340 mm/s, and a thickness of 0.15 mm) yielded noteworthy findings. The tensile performance of the specimen was confirmed through XPS analysis subsequent to the machining process and passive layer etching.

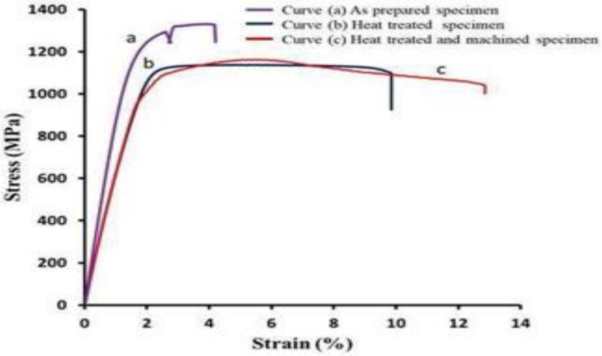

Figure 14: Specimen 27's stress-strain curve: Curve (a): As printed example, stress is 1331 MPa and elongation is 4.3%. b) Curve: Stress 1138 MPa, % Elongation 9.9%, for a piece that was heated. Curve (c): Stress 1162 MPa, Elongation 12.9%, heat-treated and machined specimen.

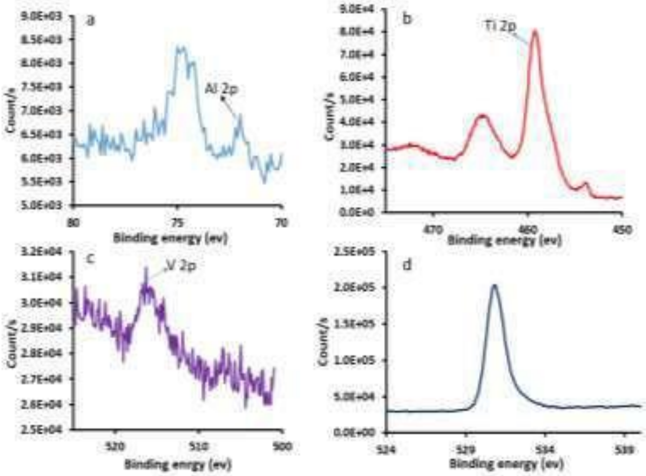

Figure 15a: XPS study spectrum of the additively made and heat-treated sample at the surface before etching (a) Aluminum (b) Titanium (c) Vanadium (d) Oxygen

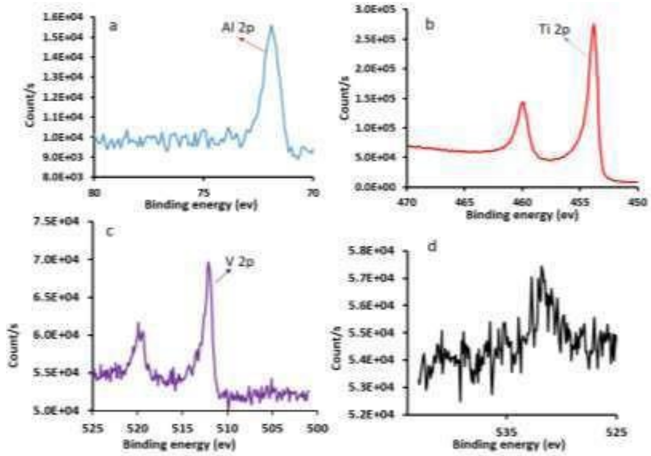

Figure 15b: XPS study spectrum of the additively made and heat-treated sample at the surface after etching (a) Al (b) Ti (c) V (d) O_2

4.2.5 SCC Results analysis

SCC of metals in corrosive settings was studied with SSRT analysis. To find the SCC of metal, slow tensile stress was done on different samples of different materials and cross-section areas. Studies of comparisons were done in both open-air and solution settings, such as 3% NaCl in water. By analysing the link between elongation in a solution and in air, it was possible to figure out how likely the metal alloy was to rust.

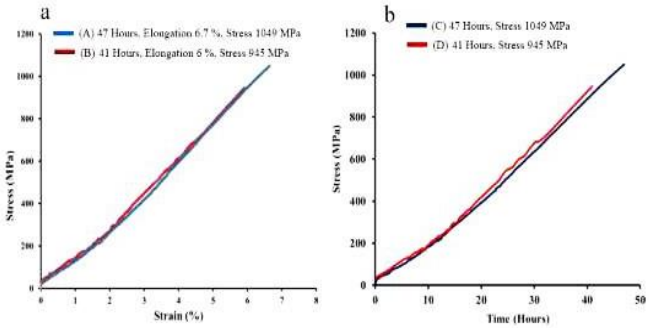

Figure 15c: (a) Stress vs Strain curve for strain rate 1 x 10(-4)-s1 of LPBF process and heat-treated Ti-6Al-4V alloy material in the NaCl solution and open-air environment and (b) Time curve vs Stress

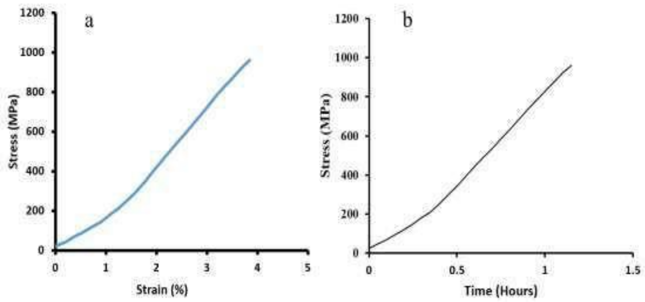

Figure 15d: Elongation vs. stress of the Ti-6Al-4V treated by LPBF and evaluated by SSRT under ambient air (open-air) conditions (b) Time vs Stress

4.3 *Corrosion test analysis*

The corrosion response of specimens composed of Ti-6Al-4V was investigated in a study, with particular emphasis placed on analyzing their microstructure. The specimens underwent testing in electrolytes consisting of 3.5% NaCl and aerated PBS, as depicted in Figure 16a. The polarization data were examined for specimens that underwent heat treatment and those that did not undergo heat treatment. The utilization of electrochemical impedance evaluation was employed to examine the corrosion resistance within the identical electrolyte solution. The results are depicted in Figures 16a, b, and c.

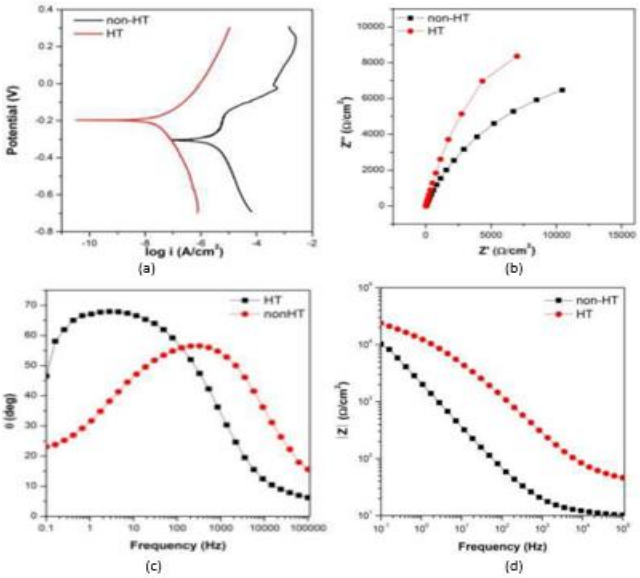

Figure 16 (a) demonstrates Tafel diagrams for Ti-6Al-4V samples in a 3.5% NaCl electrolyte (b) Nyquist diagrams for non-HT and HT samples., (c) electrochemical impedance phase angle and (d) bode plots for non-HT and HT samples.

5. CONCLUSION

The study uses laser powder bed fusion to fabricate Ti-6Al-4V alloy specimens, optimizing process parameters for industrial applications. STM and XPS techniques were used for phase transition properties and microstructural analysis. Results showed physical and mechanical attributes like tensile strength, relative density, elongation, and microhardness. Heat treatment effects on corrosion rates were examined in phosphate buffer and NaCl electrolytes.The purpose of this research was to construct a DOE L-27 General Full Factorial Design for analysing the effect of process parameters on mechanical qualities in LPBF processing. Elongation %, microhardness, and tensile strength were taken into account when fine-tuning the laser power and scan speed. The microstructural features and corrosion resistance of Ti-6Al-4V alloy samples were thoroughly examined.

Heat-treated samples exhibit a lower beta phase fraction, suggesting an a'-martensite change, and dislocation density and twins are also seen in the material.Grain size is higher in non-heated Ti-6Al-4V samples, whereas it is ultra-fine in heat-treated samples, which also exhibit lamellar and phase transformations.Plastic deformation similar to that of Ti-6Al-4V alloys may be achieved using laser technology.

Spectroscopic transmission microscopy analysis revealed a lamellar/equiaxed microstructure in a'-martensite as a result of heat treatment.

Vacancy and dislocation twins were observed in the Ti-6Al-4V alloy's hexagonal close-packed (HCP) nanostructure.

Energy density improvement led to greater tensile strength, whereas plastic deformation caused the material to stretch.

Removing the passive layer on the surface improved the material's tensile strength.

6. REFERENCES

[1] A2018 1.l-Ketan, O., R. Rowshan, and R. K. Abu Al-Rub. The correlation between the topology of 3D-printed strut, skeleton, and sheet-based periodic metallic cellular materials and their mechanical properties. 19:167–183 in Additive Manufacturing.

[2] Baca, A., R. Konecna, G. Nicoletto, and L. Kunz (2016). Direct Metal Laser Sintering-Created Ti6Al4V Alloy: How the Build Direction Affects Fatigue Behaviour. The proceedings of Materials Today, 3(4), 921-924.

[3] Brandt, Michael. 2017. Additive manufacturing and the function of lasers. Manufacturing using a Laser Additive Layer:

[4] Emmelmann, C., D. Herzog, and J. Kranz. (2017). Ten - Make it such that it can be manufactured using a laser. Electronic and optical materials, in M. B. T.-L. A. M. Brandt (Ed.), Woodhead Publishing Series in (pp. Woodhead Book Company.

[5] Frazier, William E. (2014). Review of the process of metal additive fabrication. The Materials Performance and Engineering Journal, 23, 1917-1928.

[6] Henthorne, Mark. Fifty years of data from the slow strain rate stress corrosion cracking test. As reported in Corrosion, 72(12), pages 1488-1518.

[7] Ion, John C.; Harold R. Shercliff; Michael F. Ashby (1992). Laser processing of materials diagrams. Accessed from: Acta Metallurgica et Materialia, 40(7), 1539-1551

[8] Jeong (D), Park (J), Ahn (S), Sung (H), Kwon (Y), and Kim (S) (2018). Ti-6Al-4V alloy SCC susceptibility after stabilisation annealing in 0.6 M NaCl solution. Metallurgical and Materials Transactions A 24(1), 101-111.

[9] A.M. Khorasani, I. Gibson, and U.S. G. A. Awan (2019). Ti-6Al-4V's density, hardness, tensile strength, and surface quality as a function of SLM process parameters. 25(9), (176-186), Additive Manufacturing.

[10])Koide, K., T. Anraku, A. Iwase, and H. Inoue. (2017). Ti-6Al-4V a11oy was subjected to high-pressure, high-temperature strain testing at a low strain rate in hydrogen gas. 58(6), 886-891 in Materials Transactions.

[11] Lee, H.; Lim, C.; Low, M.; Tham, N.; Murukeshan, V.; and Kim, Y. J. 11. (2017). A look at the use of lasers in additive manufacturing. Journal of Green Technology in Precision Engineering and Manufacturing, Volume 4, Issue 3, Pages 307-322.

[12] Leary, M. (2017a). Optimising surface roughness for selective laser melting (SLM): Taking into account both important and unimportant surfaces. Materials, Designs, Technologies, and Applications for Laser Additive Manufacturing. Corporate Name: Elsevier Ltd.

[13] Leary, M. Optimal surface roughness for selective laser melting (SLM): Taking into account both important and unimportant surfaces. Materials, Designs, Technologies, and Applications for Laser Additive Manufacturing. Corporate Name: Elsevier Ltd

[14] N. C. Levkulich, S. L. Semiatin, J.E. Gockel, J. R. Middendorf, A. T. DeWald, and N. W. Klingbeil. 14. (2019). Laser powder bed fusion of Ti-6Al-4V: development of residual stress and distortion as a function of processing parameters. 28(4):475-484 Additive Manufacturing

[15] Luo, X., J. Li, and M. Lucas. Technology based on galvanometer scanning for use in laser additive manufacturing. SPIE Proceedings (10095), 16.(1998). Liitjering, G. Mechanical characteristics and microstructure of (a,p) titanium alloys as a function of processing. Published in Materials Science and Engineering: A, 243(1), 32–45

[16] .Rui Liu, Ying Cui, Lan Liu, Bo Zhang, and Fei Wang. Hydrostatic pressure on stress corrosion cracking in Ti-6Al-4V alloy in 3.5% NaCl solution: a first-principles investigation. Science of Corrosion, 165(10), 802-1

[17] Liu, Z. Wang, T. Sparks, F. Liou, and J. Newkirk was published in 2017. Laser additive manufacturing in the aerospace industry. Materials, Designs, Technologies, and Applications for Laser Additive Manufacturing. Corporate Name: Elsevier Ltd.

DOI: https://doi.org/10.15379/ijmst.v10i2.3197